Desalination and Water Treatment
www.deswater.com
doi: 10.5004/dwt.2020.24916

175 (2020) 229–243
January

Development of iron oxide nanoparticles using alginate hydrogel template for chromium (VI) ions removal

A.M. Omer[a], T.M. Tamer[a], W.M. Abou-Taleb[b], G.D. Roston[c], E.F. Shehata[b], A.M. Hafez[b], R.E. Khalifa[a], M.S. Mohy Eldin[a,*]

[a]*Polymer Materials Research Department, Advanced Technology and New Materials Research Institute, (ATNMRI), City of Scientific Research and Technological Applications (SRTA-City), New Borg El-Arab City, 21934, Alexandria, Egypt, emails: mohyeldinmohamed@gmail.com (M.S. Mohy Eldin), ahmedomer_81@yahoo.com (A.M. Omer), ttamer85@yahoo.com (T.M. Tamer), randaghonim@yahoo.com (R.E. Khalifa)*
[b]*Physical Department, Faculty of Education, Alexandria University, Alexandria, Egypt, emails: wmaboutaleb@gmail.com (W.M. Abou-Taleb), eslam_fadl@yahoo.com (E.F. Shehata), ahmmed_hafez@yahoo.com (A.M. Hafez)*
[c]*Physics Department, Faculty of Science, Alexandria University, Alexandria, Egypt, email: Dr.gamal_daniel@yahoo.com*

Received 2 March 2019; Accepted 18 September 2019

ABSTRACT

Iron oxide nanoparticles (IONPs) were developed by alginate hydrogel template for chromium (VI) ions separation. The IONPs were characterized using Fourier-transform infrared spectroscopy, thermogravimetric analysis, scanning electron microscopy, transmission electron microscopy, X-ray diffraction and magnetic properties analysis. The separation efficiency of the IONPs for Cr(VI) ions investigated under initial Cr(VI) ions concentration, pH, adsorbent dosage, contact time and temperature. Furthermore, the adsorption process data were tested using different kinetic models. The isotherm nature was examined using Freundlich, Langmuir and Temkin models. Besides, the adsorption controlling step was determined using inter-particles and D-W diffusion models. The thermodynamic nature of the process was extracted using Van't Hoff plot.

Keywords: Iron oxide nanoparticles; Alginate template; Chromium (VI) removal

1. Introduction

Recently, covering the demands of the clean water for the domestic and the industrial uses presents a real challenge all over the world. The estimated world consumption of freshwater in 2025 is around 3.8 times the world consumption in 1950. Only 16.65% of this demand is expected to be available by that time, which is a clear example of severe water scarcity problem [1]. Half of the world population has to face this problem by the year 2025, and a negative effect on economic development is much more expected as a result. Increasing the water resources has to be done in the direction of solving the problem. Treatment of the wastewater for possible reuse is one of the proposed strategies to increase water resources [2].

One of the main sources of water contamination is the heavy metal ions released into natural water by human activities [3]. Toxicity of the heavy metal ions found depends on its oxidation state [4]. A common industrial wastewater contaminant is chromium ions released by varied industries as two oxidation states; Cr(III) and Cr(VI). The higher oxidation state (Cr; VI) is highly toxic and causes a wide range of health problems [5,6]. Main concerns about the cost and efficiency of the conventional methods are raised [7–10]. These treatment methods can be classified as chemical, physical and biological. They are often selected based on many

* Corresponding author.

advantages such as high selective separation, simplicity in control, and lower space requirement. Physico-chemical treatments can be considered to be the most suitable treatment methods for the removal of metal ions from industrial wastewater. However, they still suffer from high operating cost due to the high price associated with the chemicals used and high energy consumption. Overall, each treatment method has its advantages and limitations. The main advantages and disadvantages of the different physico-chemical treatments have been discussed in the published review by Al-Saydeh et al. [11]. Nanomaterials have many advantages as adsorbent materials which present a possible solution for the drawbacks of conventional treatment strategies [12]. However, separation of nanomaterials from the medium is a challenge which leads to the use of magnetic nanoparticles. Magnetic iron oxide-based nanoparticles received increased attention in the last decade [13] for the treatment of wastewater [14]. The design and synthesis of such nanoparticles have centered on techniques such as sol-gel [15], chemical coprecipitation [16], microemulsion [17], etc. Most of these techniques result in aggregation of nanoparticles during synthesis. Copolymer templates have been efficiently used to host chemical reactions. They have the advantage of avoiding nanoparticle clustering and also providing stable frameworks against chemical degradation [18]. Use of copolymer templates has been reported for the synthesis of iron oxide nanoparticles (IONPs) such as maghemite [19], cobalt ferrite [20] and magnetite [21]. There is an increasing interest in the use of green resources for nanoparticle synthesis. Starch has been reported as a capping agent during the preparation of iron oxide. Ferric salts precipitated as its hydroxide using triethylamine [22], or by precipitating a mixture of ferric and ferrous salts [23]. Polysaccharides have also been employed to modify the surface characteristics of the nano-iron oxides generated [24]. Carp et al. [25] reviewed the main developed synthetic routes of oxide materials with a special emphasis on the gel-template ones using alginate as an efficient raw material. Plumejeau et al. [26] briefly review the recent advances in metal oxide preparation by mineralization process of biopolymers such as cellulose, starch, alginate, chitosan, chitin, carrageenan, dextran, DNA, pectin, collagen, gelatin, silk, lignin and white-egg. Ali et al. [27] reviewed recent information from synthesis to characterization, and applications of iron NPs. The review summarizes the methods for the preparation of iron oxide NPs, size and morphology control, and magnetic properties with recent bioengineering, commercial, and industrial applications. Nidhin et al. [28] reported the preparation of nanoparticles of iron oxide in the presence of chitosan and starch biopolymer templates. The particle size distribution was uniform, and particles were more or less monodisperse for chitosan and starch template-assisted synthesis. The iron oxide synthesized was crystalline and matched with that of hematite. Janardhanan et al. [29] investigated natural polymers such as chitosan and starch as templates for the preparation of IONPs. The templates offer selective binding sites for Fe(II) under aqueous conditions. Controlled drying and subsequent removal of the template backbone enables the synthesis of spatially separated IONPs. The crystalline character of the IONPs and near narrow particle size distribution were recognized. Earlier reported methodologies where natural polysaccharides and polymers have employed for encapsulation or capping of iron oxides synthesized by precipitation methods [22–24,30]. This work uses alginate as a template in the template surface method. The binding and separating of the Fe(II) centre to carboxylic and hydroxyl groups in the alginate polymer which subsequently converted to the corresponding oxide by calcination was reported. The developed nanoparticles were characterized using different characterization tools such as Fourier-transform infrared spectroscopy (FT-IR), thermogravimetric analysis (TGA), X-ray diffraction (XRD), magnetic properties and particles size analysis. Finally, the iron oxide nanoparticles (IONPs) were evaluated for Cr(VI) removal from aqueous solutions under different operational conditions. The adsorption data were fitted using different kinetic and isotherm models. Moreover, the thermodynamics of the adsorption process was studied.

2. Materials and methods

2.1. Materials

1,5-Diphenylcarbazide and sodium alginate ($C_6H_7O_6Na$) medium viscosity purchased from Alpha chemika, India. Iron (III) nitrate ($Fe(NO_3)_3 \cdot 9H_2O$) and potassium dichromate ($K_2Cr_2O_7$) were purchased from Sigma-Aldrich (USA).

2.2. Methods

2.2.1. Iron oxide nanoparticles development

Equal portions of sodium alginate solution (4%) were mixed with iron nitrate solution (4%) using homogenizer to obtain a homogeneous hydrogel slurry. The slurry was then filtered and washed with distilled water to remove un-trapped iron nitrate. After that, the iron-alginate hydrogel was dried in a dryer at 60°C overnight. Finally, the dried iron-alginate particles were calcinated in an oven at 800°C for 3 h to have IONPs.

2.2.2. Iron oxide nanoparticles characterization

2.2.2.1. Fourier-transform infrared spectroscopic analysis

The structures of IONPs were investigated by FT-IR using Fourier-transform infrared spectrophotometer (Shimadzu FTIR - 8400 S, Japan).

2.2.2.2. Thermal gravimetric analysis

TGA of IONPs was carried out using a thermogravimetric analyzer (Shimadzu TGA-50, Japan). The temperatures ranging from 25°C to 800°C under nitrogen atmosphere at a gas flow rate of 20 mL/min and a heating rate of 10°C/min.

2.2.2.3. Particle size analysis

0.1 g of IONPs were dispersed in 10 mL distilled water. Each sample was sonicated using an ultrasonic water bath for 15 min before being measured in a submicron particle size analyzer (Beckman Coulter N5, USA).

2.2.2.4. Scanning electron microscope

Scanning of IONPs was examined using a scanning electron microscope (JEOL JSM 6360LA, Japan).

2.2.2.5. Transmission electron microscope

IONPs were carried out using transmission electron microscope (JEOL JEM-100CX) is a tungsten-filament. A magnification from 100x to 250,000x and a resolution power of 0.2 nm were provided (Faculty of Science – Alex University, Egypt).

2.2.2.6. X-ray diffraction

The crystallinities of IONPs were investigated by X-ray diffraction (XRD) analysis using (Shimadzu, XRD-7000) diffractometer. X-ray diffractometer was adopted to investigate the solid-state morphology of IONPs.

2.2.2.7. Magnetic property

Magnetic measurement was done using a SQUID magnetometer (MPMSXL-7, Quantum Design, USA). Magnetization curves were recorded for a suspension and solid sample of SPION-alginate at 27°C with an applied magnetic field up to 10,000 Oe.

2.2.3. Chromium ions separation

The separation of the Cr(VI) ions from synthetic solution was conducted under batch adsorption conditions. IONPs (0.1 g) were mixed with 25 mL of Cr(VI) solution (25 mg/L) of pH 2.0 for 4 h at 30°C. The chromium (VI) concentration in the samples was determined by measuring the optical density of the formed purple complex with 1,5-diphenylcarbazide at 540 nm by UV spectrophotometer. The chromium removal (%) was determined according to the following equation:

$$\text{Removal}\left(\%\right)=\frac{\left(C_0-C_e\right)}{C_0}\times 100 \quad (1)$$

where C_o is the initial concentration and C_e is the concentration at equilibrium.

The removal capacity is calculated according to the following formula:

$$q\left(mg/g\right)=\frac{V\left(C_0-C_t\right)}{M} \quad (2)$$

where q is the uptake capacity (mg/g); V is the volume of Cr(VI) solution (mL) and M is the mass of IONPs (g).

3. Results and discussion

3.1. Characterization

3.1.1. FT-IR

Fig. 1 exhibits FT-IR of IONPs developed using alginate as a template. The spectrum shows the active band at 475 cm^{-1}, which is attributed to α-Fe_2O_3 [29]. The chart also demonstrates absorption bands at 602 cm^{-1} assigned to vibration of Fe–O bond which is in agreement with the literature values [31,32], C–H stretching vibrations at 1,033 cm^{-1} [33,34] and at 2,925 cm^{-1} [29], C–O bending at 2,359 cm^{-1} and O–H stretching at 3,354 cm^{-1}. The absorption band at 3,354 cm^{-1} appeared due to absorption of moisture by nanoparticles from the environment [35].

3.1.2. Thermal gravimetric analysis

Thermal gravimetric analysis of the prepared IONPs was performed and presented in Fig. 2. The weight loss that is observed at temperature ranged between room temperature and 200°C can be attributed to the loss of the moisture content attached to the surface of the particles. The absence of a significant weight loss at higher temperature confirmed that there is no residue of polymeric template attached to prepared particles.

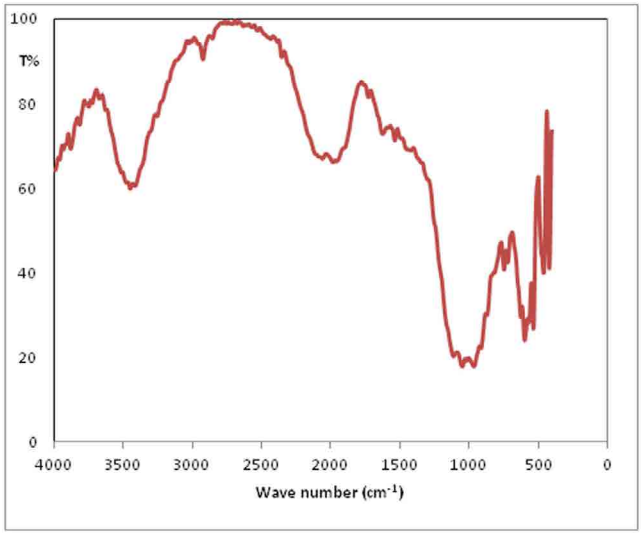

Fig. 1. FTIR of the iron oxide nanoparticles.

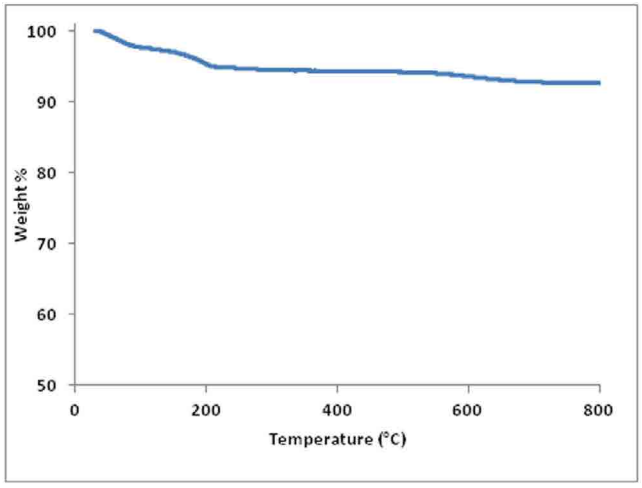

Fig. 2. Thermal gravimetric analysis of the iron oxide nanoparticles.

3.1.3. Particle size analysis

Different sizes of the IONPs were obtained using different calcination temperature (Table 1). From the table, it can be seen that the elevation of the calcination temperature has a reducing effect on the particles size. The size reduced from 166 nm at 500°C to 39.8 nm at 800°C. That finding is in contrast with previous results using phosphonate alginate as a template [36].

3.1.4. Scanning electron microscope

Fig. 3 shows a scanning electron microscopy (SEM) image of the synthesized IONPs confirming that the particles obtained were in the nanometer range. Also, the picture demonstrates the spherical structure of particles. Different size of particles may be attributed to the accumulations of prepared nanoparticles.

3.1.5. Transmission electron microscope

Transmission electron microscopy (TEM) was carried out to determine the morphology of prepared IONPs. The typical TEM image of IONPs was shown in Fig. 4. The diameter of particles shows that most of the particles are below 10 nm; however, the right shape and size of particles could not be defined as the particles agglomerated.

3.1.6. X-ray diffraction

XRD analyses confirmed that the synthesized nanoparticles were magnetite (Fe_3O_4), as shown in Fig. 5. There are seven characteristic peaks of 2θ, 33.28, 35.76, 49.64, 54.22, 57.72, 62.56 and 64.14 and the corresponding intensities (*I*) with height are 442, 384, 370, 416, 362, 386 and 398, respectively. In the pattern of XRD diffraction, the broad nature of the diffraction bands indicated that Iron oxide have small particle sizes.

3.1.7. Magnetic properties

The hysteresis loop of IONPs measured in the maximum applied the field of 15 × 109 E + 3 Oe at room temperature shown in Fig. 6. The saturation magnetizations were 36.3 emu/g. The large saturation magnetization and superparamagnetic property of the prepared nanoparticles made it susceptible to the magnetic field and quickly separated from a liquid phase.

Table 1
Particles size of the iron oxide nanoparticles prepared using different calcinations temperature (2% alginate, 2% iron nitrate and 3 h calcination time)

Calcination temperature (°C)	Particle size (nm)
500	166.3
600	96.1
700	62.2
800	39.8

3.2. Separation of chromium (VI) ions

Recently, there is a fast-growing interest in using iron oxide nanomaterials for heavy metal removal. Collection of nanoparticles using magnetic field after treatment in wastewater simplified its application. In the current study, Cr(VI) is used as a heavy metal pollutant model. Several factors can be affected by the adsorption process, such as contact time, solution pH, temperature, initial Cr(VI) concentration, adsorbent dosage. In addition to these factors, the effect of the nanoparticle size on the adsorption performance has

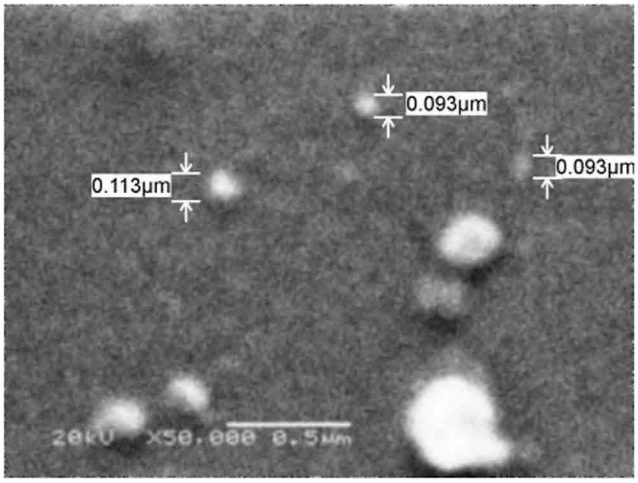

Fig. 3. SEM photograph of the iron oxide nanoparticles.

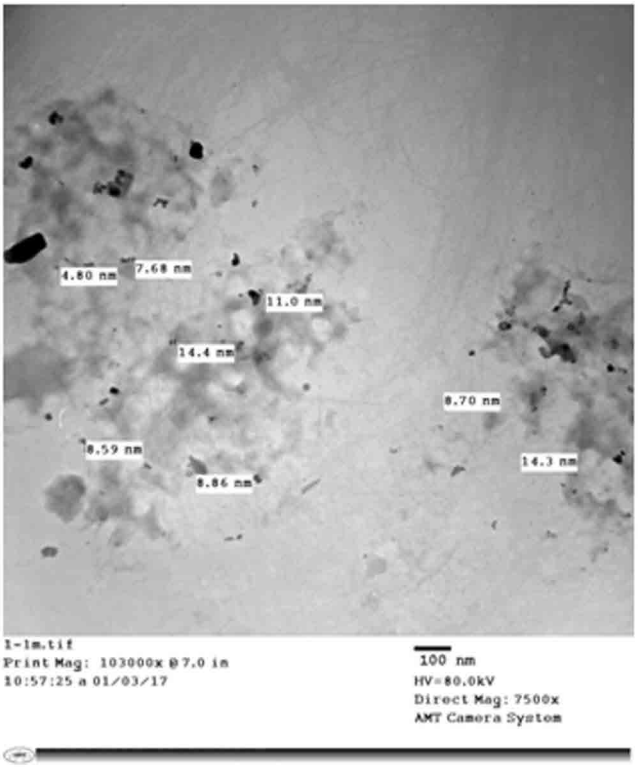

Fig. 4. TEM photograph of the iron oxide nanoparticles.

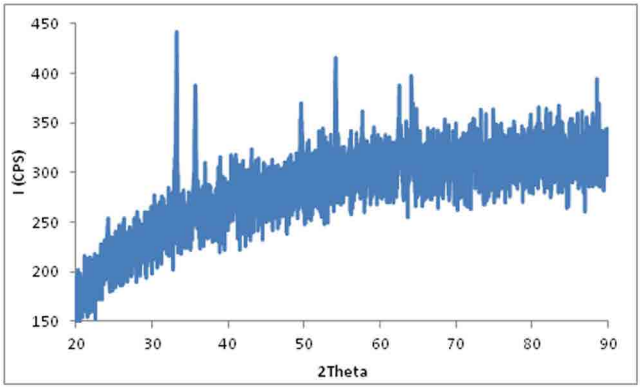

Fig. 5. XRD pattern of the iron oxide nanoparticles.

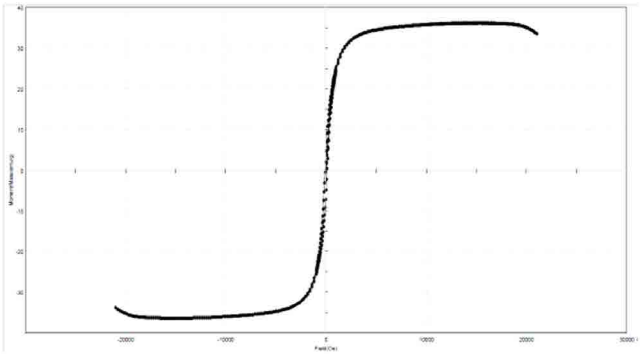

Fig. 6. VSM measurements of the Iron oxide nanoparticles.

been studied [37]. The results of these factors were discussed below. Moreover, the kinetic, isotherm and diffusion behaviour of the adsorption process of the Cr(VI) ions onto IONPs were studied. Finally, the thermodynamic parameters of the adsorption process were calculated.

3.2.1. Effect of the adsorption time

Fig. 7 shows the effect of varying the adsorption time on the adsorption capacity of the IONPs. From the value, it is clear that the adsorption capacity increased linearly with the adsorption time within the studied range. That trend gives an indication of the availability of adsorption centres on the IONPs surface. However, only 28% of the Cr(VI) ions were removed after 4 h. Kitkaew et al. [38] observed that the amounts of Cr(VI) removal elevated with increasing contact times, where removal efficiency of Cr(VI) by the IONPs was initially high, being 60% and 80% after the contact times of 1 and 30 min, respectively, and then slowed down to 86% at the contact time of 120 min. That reflects that more significant numbers of adsorptive sites were available for adsorbate during the initial short contact times [38]. The obtained results in our study emphasize the limited quantities of adsorptive sites available on the IONPs surface and nominate the occurring of the adsorption for the Cr(VI) ions mainly on the pores internal surface. This explanation supported by the fact that the IONPs size in our case is 40 nm while it is below 10 nm in Kitkaew et al. [38] study.

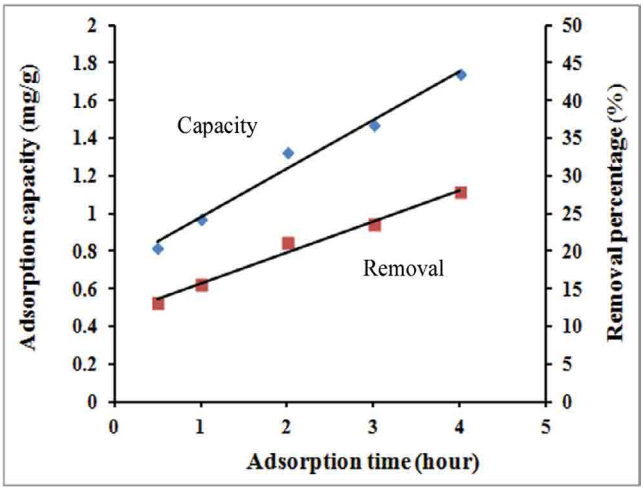

Fig. 7. Effect of the adsorption time on the adsorption capacity of IONPs (iron oxide nanoparticles [0.1 g], 25 mL of Cr(VI) solution [25 mg/L] of pH 2.0, 0.5–4 h adsorption time and 30°C adsorption temperature).

3.2.2. Effect of the chromium (VI) ions concentration

The impact of the initial Cr(VI) ions concentration varying on the adsorption capacity of the IONPs shown in Fig. 8. The figure demonstrated that the adsorption capacity increased linearly with the initial Cr(VI) ions concentration up to 25 ppm. After that, the adsorption capacity increment starts to level off and got stabilized at 100 ppm. The levelling off the adsorption capacity is an indication of the saturation of the IONPs with the Cr(VI) ions. On the other hand, removing percentage decreased by increasing the initial Cr(VI) concentration, which is in agreement with literature findings by Shirsath et al. [39]. That might be because of the fact that with an increase in the initial concentration of the metal, the number of metal ions adsorbed on the surface of Fe_2O_3. Thus increase in the several substrate ions accommodating in interlayer spacing inhibits the adsorption, which thereby decreases the reactive site of Fe_2O_3 result of that decrease in removal of chromium ions by Fe_2O_3 as the concentration of metal ions increases. Al-Saad et al. [40] tested the iron oxide (α-Fe_2O_3) nanoparticles and its applicability to purify water from the aluminium (Al III), arsenic (As III), cadmium (Cd II), cobalt (Co II), copper (Cu II), and nickel (Ni II) where they found that increasing the concentration of the metal did not affect much the adsorption of the metal As(III) and Cu(II) and their removal percentage remained around 95% for both. On the other hand, a dramatic decrease of the removal percentage for both cobalt and nickel was observed under the same conditions which refer to the effect of the metal ions type [40].

3.2.3. Effect of the adsorption pH

The pH of the solution is an essential parameter which controls the adsorption process. It affects the ionization of the adsorptive molecule and therefore, the surface charge of the adsorbent. Consequently, studying the effect of pH on the adsorption process is essential in adsorption analyses.

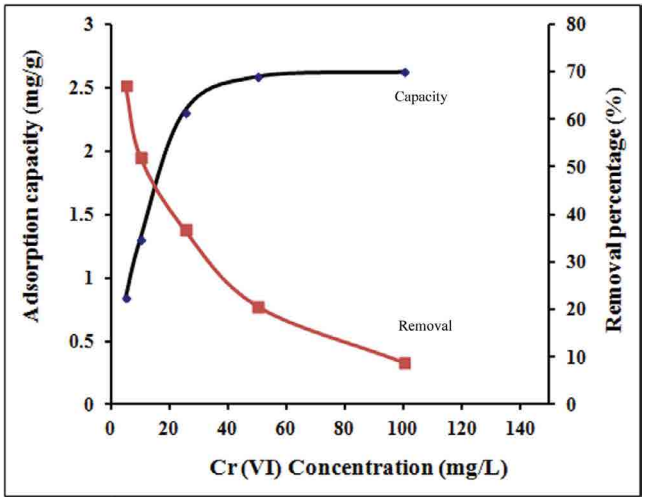

Fig. 8. Effect of the Cr(VI) ions concentration on the adsorption capacity of IONPs (iron oxide nanoparticles [0.1 g], 25 mL of Cr(VI) solution [5–100 mg/L] of pH 2.0, 4 h adsorption time and 30°C adsorption temperature).

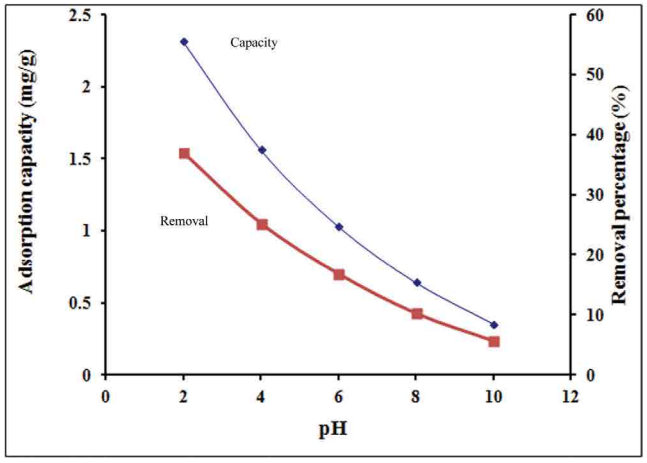

Fig. 9. Effect of the adsorption pH on the adsorption capacity of IONPs (iron oxide nanoparticles [0.1 g], 25 mL of Cr(VI) solution [25 mg/L] of pH [2.0–10.0], 4 h adsorption time and 30°C adsorption temperature).

In this particular case, the solution pH can change the surface charge of the adsorbent as well as different ionic forms of chromium.

Fig. 9 shows the effect of varying the Cr(VI) ions solution pH on the adsorption capacity of the IONPs. The figure demonstrates an inverse relationship which the highest adsorption capacity and removing percentage was obtained at the lowest pH and then dramatically decreased with pH increase (i.e., decay curve). The same trend was obtained by other authors [41].

Chromium (VI) ions exist in the anionic forms ($Cr_2O_7^{2-}$, $HCrO_4^-$ or CrO_4^{2-}) in water depending on the pH and concentration. In highly acidic media (pH < 1), the Cr(VI) ions exist mostly as H_2CrO_4 (pK_1 = 6.51 and pK_2 = 5.65). At pH between 2 and 6, there is an equilibrium between $Cr_2O_7^{2-}$ and $HCrO_4^-$ ions. Under alkaline conditions (pH > 8), it exists predominantly as chromate anions. The equilibrium between chromate and dichromate ions in water can be shown by the following equation [42]:

$$Cr_2O_7^{2-} + H_2O \rightleftarrows 2CrO_4^{2-} + 2\,H^+ \quad (3)$$

The optimum pH for adsorption of Cr(VI) onto different nano sorbent is within the 2–3 range. That can be attributed to the presence of Cr(VI) in various ionic forms in the solution at different pH values. $HCrO_4^-$ is the predominant species at pH = 2–3 range, and it is readily adsorbed due to the low adsorption free energy [43]. On the other hand, a dramatic decrease in adsorption was observed in most cases when increasing the pH value [44,39]. This may be attributed to few reasons, mainly, the competition with hydroxyl ions for the adsorbent sites and the change of surface charge of the adsorbent leading to electrostatic repulsion between adsorbent and Cr(VI) anions leading to release of already adsorbed ions [45], as well as some of the trivalent cations, that may react with OH− ions and precipitated and thereby decreased the free metal ions available in the solution [46].

3.2.4. Effect of the adsorption temperature

Effect of varying the adsorption temperature on adsorption capacity was studied and is presented in Fig. 10. The figure revealed that increasing the adsorption temperature, in the studied range from 25°C to 50°C, increased the adsorption capacity slightly from 2.1 to 2.6 mg/g. The removal percentage shows the same behaviour, which rose from 34% to 42%. A study carried out by Shen et al. [47] on the adsorption of the elements (Cu^{2+}, Cr^{6+}, Ni^{2+} and Cd^{2+}) by Fe_3O_4 showed a similar result, in which the adsorption of metals increases as temperature increased. This phenomenon can be explained by the increase of kinetic energy of ions at a higher temperature which leads consequently to increase in the collision of ions and particles [47].

3.2.5. Effect of the adsorbent dosage

The adsorbent dosage is another significant parameter in the study of the adsorption capacity of an adsorbent. The determination of the impact of adsorbent dosage gives an idea about the minimum amount of adsorbent need to be used for the adsorption process. This value is useful in the viewpoint of cost. The effect of varying the IONPs dose on its adsorption capacity and the removal percentage was studied and is presented in Fig. 11. A slight increase of the capacity was recognized with increase the dosage from 0.025 to 0.1 g. After that, further improvement of the dose was companied with a decrease in the adsorption capacity. On the other hand, the removal percentage was continuously found to increase with the increase of the adsorbent dose to reach the highest value (64%) using 0.3 g. That may be due to the availability of active adsorption sites which adsorbate can adsorb. The obtained results are in agreement with the literature [39–41].

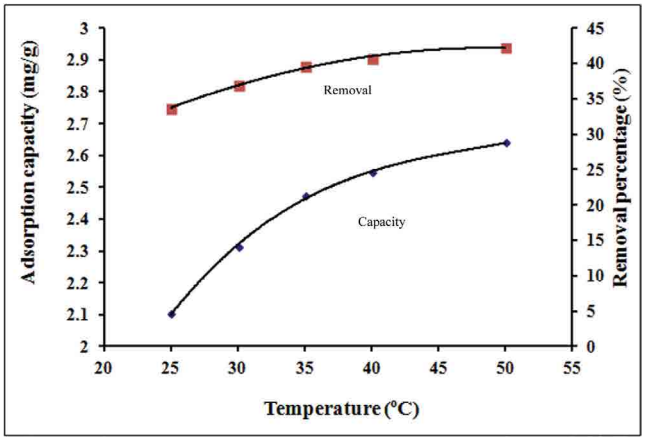

Fig. 10. Effect of the adsorption temperature on the adsorption capacity of IONPs (iron oxide nanoparticles [0.1 g], 25 mL of Cr(VI) solution [25 mg/L] of pH 2.0, 4 h adsorption time and [25°C–50°C] adsorption temperature).

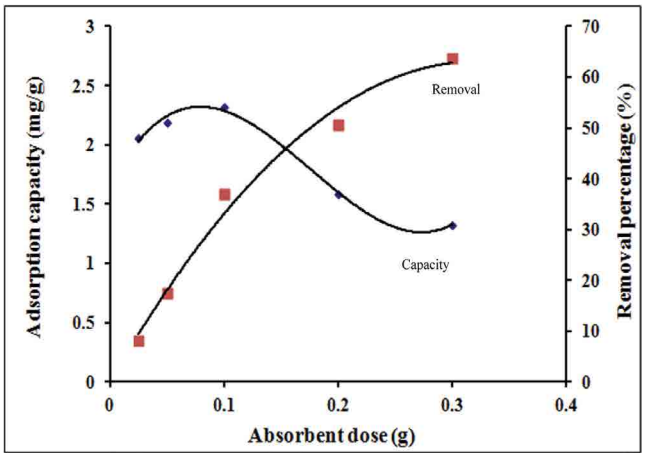

Fig. 11. Effect of the adsorbent dosage on the adsorption capacity of IONPs (iron oxide nanoparticles [0.025–0.3 g], 25 mL of Cr(VI) solution [25 mg/L] of pH 2.0, 4 h adsorption time and 30°C adsorption temperature).

3.2.6. Effect of the adsorbent particles size

The impact of the IONPs size variation on the adsorption capacity and the removal percentage has been explored (Fig. 12). From Fig. 12, it is clear that the particles size has a direct impact on the adsorption capacity of the IONPs and the removal percentage of the Cr(VI) metal ions. An inversely proportional relation has been realized from the figure where the increment of the adsorption capacity of the IONPs and the removal percentage of the Cr(VI) metal ions is accompanied with a decrease of the particles size. This relation is a linear one in the particles size between 166 and 96 nm, then turned to be exponential one with particle size below 96 nm where the capacity increases from 1.1981 to 1.7369 mg/g for 96 and 39.8 nm particles. This behaviour is closely related to the rise of the contacted surface area of the IONPs with the Cr(VI) anions solution.

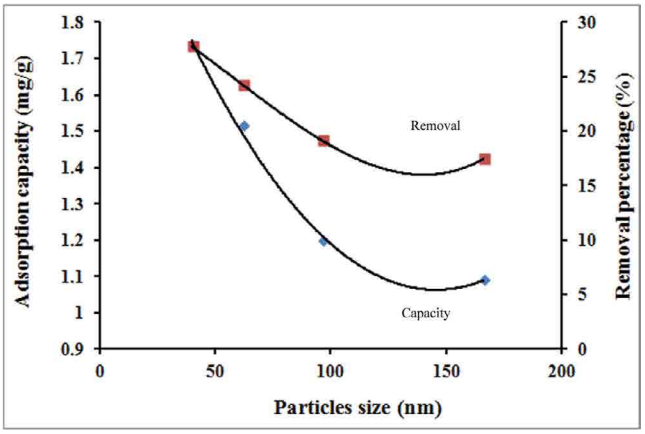

Fig. 12. Effect of the IONPs size on its adsorption capacity [Iron oxide nanoparticles (0.1 g), 25 mL of Cr(VI) solution (25 mg/L) of pH 2.0, 4 h adsorption time and 30°C adsorption temperature].

3.3. Adsorption isotherm studies

Adsorption isotherms are mathematical models that describe the distribution of the adsorbate species among solid and liquid phases and are thus crucial from the chemical design point of view. The results obtained on the adsorption of the Cr(VI) anions onto the IONPs were analyzed by the well-known models given by Freundlich, Langmuir and Temkin. The sorption data obtained for equilibrium conditions have been analyzed by using the linear forms of these kinds of isotherms.

The Freundlich isotherm is a widely used equilibrium isotherm model but provides no information on the monolayer sorption capacity, in contrast to the Langmuir model [48,49]. The Freundlich isotherm model assumes neither homogeneous site energies nor limited levels of sorption. The Freundlich model is the earliest known empirical equation and is shown to be consistent with an exponential distribution of active centres, characteristic of heterogeneous surfaces [50].

$$\ln q_e = \ln K_F + \frac{1}{n_f}\ln C_e \tag{4}$$

where K_F is the Freundlich constant depicts adsorption capacity, and n_f is a constant indicating adsorption intensity. With plotting $\ln q_e$ against $\ln C_e$, a straight line with slope $1/n_f$ and intercept $\ln K_F$ obtained. The intercept of the line, K_F, indicates roughly of the adsorption capacity with slope, n, as an indicator of adsorption effectiveness. For the adsorption isotherms, the initial Cr(VI) anions concentration was varied while the pH and temperature of the solution, the agitation speed and adsorbent weight in each sample were held constant.

Linear fits of sorption data of the Cr(VI) anions are given in Fig. 13a. According to the correlation coefficient (R^2) value (0.906), it was demonstrated that the removal of the Cr(VI) anions using IONPs obeyed the Freundlich isotherm. The values of Freundlich constants n_f and K_F that were estimated from the slope and intercept of the linear plot were 3.349 and 0.8105 (Table 2). From the estimated value of n_f,

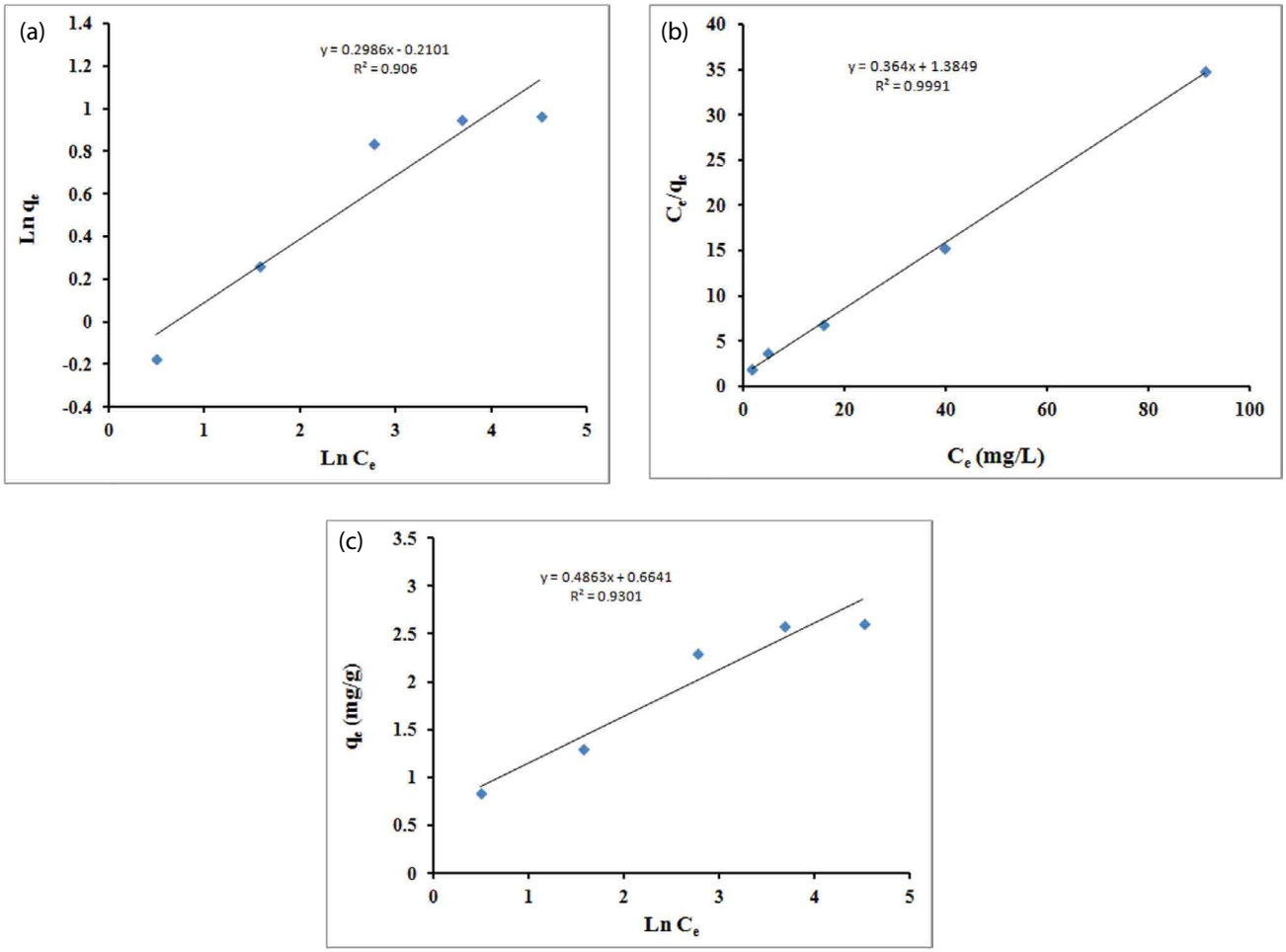

Fig. 13. Adsorption isotherm models: (a) Freundlich, (b) Langmuir, and (c) Temkin.

it was found that $n_f > 1$ indicating favourable adsorption for the Cr(VI) anions using IONPs [51].

The Langmuir equation, which is valid for monolayer sorption onto a completely homogeneous surface with a finite number of identical sites and with negligible interaction between adsorbed molecules, is given by the following equation [52]:

$$\frac{C_e}{q_e} = \frac{1}{q_m K} + \frac{C_e}{q_m} \tag{5}$$

where q_e is the amount adsorbed (mg/g), C_e is the equilibrium concentration of the adsorbate ions (mg/L), and q_m and K are Langmuir constants related to maximum adsorption capacity (monolayer capacity) (mg/g) and energy of adsorption (L/mg).

Plotting C_e/q_e vs. C_e indicates a straight line with $1/q_m$ slope and an intercept of $1/q_m K$. Fig. 9b illustrates the linear plot of the Langmuir equation for the Cr(VI) anions removal using IONPs at various initial Cr(VI) anions concentrations. The value of correlation coefficient (R^2) is considered an indicator of the goodness-of-fit of experimental data on the isotherm's model. The R^2 value was 0.9991, indicating an excellent mathematical fit of the adsorption data.

Langmuir parameters (q_m and K) for the Cr(VI) anions removal were calculated from the slope and intercept of Fig. 13b. It was found that the computed value of q_m is equal to 2.75 mg/g and K is equivalent to 3.805 L/mg (Table 2). That indicates that the IONPs have high efficiency and low energy of adsorption for the Cr(VI) anions removal.

To predict whether an adsorption system is favourable or unfavourable, dimensionless separation factor, which is considered as an essential characteristic of the Langmuir isotherms, is calculated. R_L is defined as [53]:

$$R_L = \frac{1}{1 + KC_0} \tag{6}$$

Values of R_L (Table 3) for the Cr(VI) anions removal falling between zero and one show favourable adsorption [54], which confirmed that the adsorption of the Cr(VI) anions onto the IONPs under the conditions used in this study was favourable by Langmuir isotherm.

Temkin isotherm considered the effects of indirect adsorbent/adsorbate interactions on the adsorption process. The heat of adsorption of all the molecules in the layer would decrease linearly with coverage due to adsorbent/adsorbate

interactions [55]. It can be expressed in the linear form as [56,57]:

$$q_e = B \ln K_T + B \ln C_e \quad (7)$$

A plot of q_e vs. lnC_e (Fig. 13C) enables the determination of the isotherm constants B and K_T from the slope and the intercept. From Fig. 13c, the calculated K_T is equal to 3.92 L/g, which represent the equilibrium binding constant corresponding to the maximum binding energy. The constant B that is equal to 0.4863 J/mol is related to the heat of adsorption (Table 2).

Considering the R^2 values for the three isotherm models, the Langmuir isotherm model gave the highest R^2 value (0.9991), showing that the Cr(VI) anions adsorption onto the IONPs was best described by this model suggesting the formation of mono-layers of adsorption [52].

3.4. Adsorption kinetic models

Adsorption is a physiochemical process that involves the mass transfer of a solute (adsorbate) from the liquid phase to the adsorbent surface.

A study of the kinetics of adsorption is desirable as it provides information about the mechanism of adsorption, which is essential for an efficient process.

The most common models used to fit the kinetic sorption experiments are Lagergren's pseudo-first-order model (Eq. (8)) [55], pseudo-second-order model (Eq. (9)) [56], and Elovich model (Eq. (10)) [58].

$$\ln\left(q_e - q_t\right) = \ln q_e - k_1 t \quad (8)$$

$$\frac{t}{q_t} = \frac{1}{k_2 q_e^2} + \frac{t}{q_e} \quad (9)$$

$$q_t = \alpha + \beta \ln t \quad (10)$$

where q_e (mg/g) and q_t (mg/g) are the amount of dye adsorbed at equilibrium and at time t, respectively. k_1 (min^{-1}) and k_2 (g mg^{-1} min) are the pseudo-first-order and pseudo-second-order adsorption rate constants, respectively. The Elovich constants are α (mg/g min), the initial sorption rate, and β (g/mg) the extent of surface coverage and activation energy for chemisorption.

3.4.1. Pseudo-first-order model

The pseudo-first-order kinetic model was the earliest model about the adsorption rate based on the adsorption capacity. The value of the pseudo-first-order constant (k_1; 0.5107) and correlation coefficient (R^2; 0.9941) was obtained from the slope of the plot ln (q_e–q_t) vs. time in Fig. 14a. It indicated that the correlation coefficients are excellent. However, the estimated value of q_e was calculated from the equation; 1.21 mg/g differs from the experimental value, 1.7369 mg/g; Table 4.

3.4.2. Pseudo-second-order model

The experimental kinetic data were further analyzed using the pseudo-second-order model. By plotting t/q_t against t for Cr(VI) anions, a straight line was obtained and the second-order rate constant (k_2; 0.488) and q_e value (2.08 mg/g) were determined from the slope and intercept of the plot, Fig. 14b. The value of the correlation coefficient (R^2) is equal to 0.9767 (Table 4). Accordingly, the kinetics of Cr(VI) anions adsorption can be described well by first-order equation; however, the q_{cal} value is far from the experimental one. On the other hand, the q_{cal} value by the second-order equation is much closer to the experimental one. The findings of this investigation are in agreement with different published results that investigated the adsorption of Cr(VI) anions by ZeoliteNaX and activated carbon [59,60].

3.4.3. Elovich model

The simple Elovich model is one of the most useful models for describing the kinetics of chemisorption of

Table 2
Adsorption parameters values for the MB removal with the different studied equilibrium isotherms

Isotherm model	Parameters		
Langmuir	K_L (L/g)	q_{max} (mg/g)	R^2
	3.805	2.75	0.9991
Freundlich	K_F (mg/g)	n	R^2
	0.8105	3.349	0.906
Temkin	K_T (L/g) 3.92	B_t (J/mol) 0.4863	R^2 0.9301

Table 3
R_L values for different initial Cr(VI) anions concentrations

C_o (ppm)	R_L
5	0.05
10	0.026
25	0.0104
50	0.00523
100	0.00262

Table 4
Adsorption parameters of the pseudo-first, the pseudo-second order and the Elovich kinetic models

Pseudo-first-order				Pseudo-second-order			Elovich		
$q_{e,exp}$ (mg/g)	$q_{e,cal}$ (mg/g)	K_1 (min^{-1})	R^2	$q_{e,cal}$ (mg/g)	K_2 (m^2 mg^{-1} min^{-1})	R^2	β (g/mg)	α (mg/g min)	R^2
1.7369	1.21	0.5107	0.9941	2.08	0.488	0.9767	0.4136	1.0485	0.961

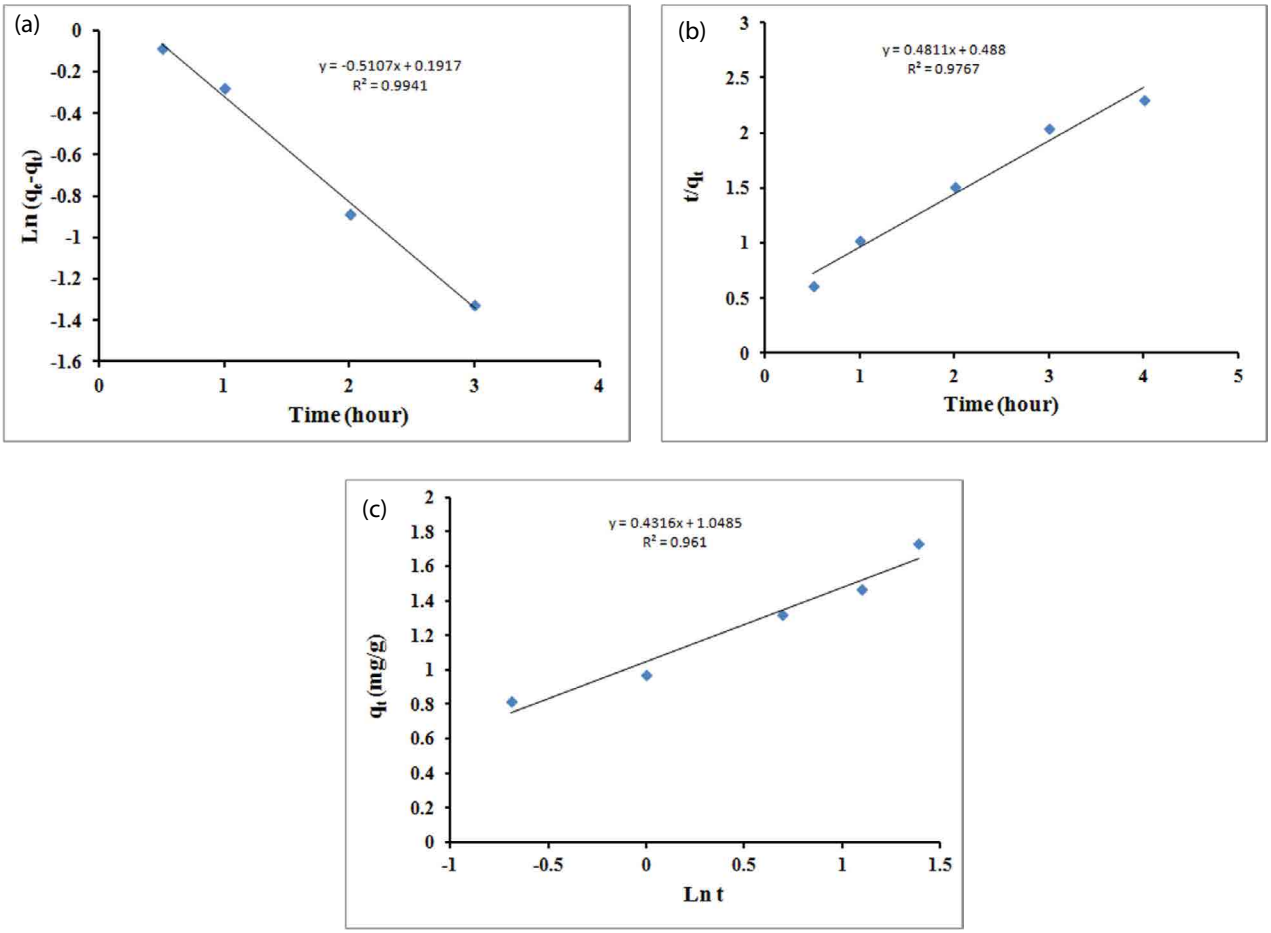

Fig. 14. Adsorption kinetic models: (a) pseudo-first-order model, (b) pseudo-second-order model, and (c) Elovich model.

gas onto solid systems. However, recently, it has also been applied to describe the adsorption process of pollutants from aqueous solutions. Fig. 14c illustrates the plot of q_t against ln$t$ for the sorption of the Cr(VI) anions onto the IONPs. From the slope and intercept of the linearization of the simple Elovich equation, the estimated Elovich equation parameters were obtained. The value of β is indicative of the number of sites available for adsorption (0.4136) while α value (1.0485 mg/g) is the adsorption quantity when ln$t$ is equal to zero; that is, the adsorption quantity when t is 1 h. The value of α (1.0485 mg/g) is very close from the experimental value; 0.9725 mg/g. This value helps understand the adsorption behaviour of the first step [61]. Also, from this figure, it is clear that the Elovich equation fits very well with the experimental data (R^2 0.961); Table 4.

3.5. Adsorption mechanism models

Following up, the adsorption mechanism of any ions onto solid from aqueous phase is going through a multi-step process. Initially, two steps were recognized in the liquid phase. The first step is the transport of the ions from the aqueous phase to the surface of the solid particles, which is known as bulk diffusion. This step is followed by diffusion of the ions via the boundary layer to the surface of the solid particles (film diffusion). The last step, consequently, happened in the solid phase where the ions transport from the solid particles surfaces to its interior pores, known as pore diffusion or intraparticle diffusion. This step is likely to be slow, and therefore, it may be considered as the rate-determining step.

Adsorption of an ion at an active site on the solid phase surface could also occur through a chemical reaction such as ion exchange, complexation and chelation.

The diffusion rate equations inside particulate of Dunwald–Wagner and intraparticle models were used to calculate the diffusion rate of the Cr(VI) anions onto the IONPs. Usually, the adsorption process is controlled by either the intraparticle (pore diffusion) or the liquid-phase mass transport rates (film diffusion) [62]. Experimenting in a batch system with rapid stirring left the possibility that intraparticle diffusion is the rate-determining step [63]. Weber and Morris [64] explored the possibility of affecting the adsorption process via intraparticle diffusion resistance using the intraparticle diffusion model described as follows:

$$q_t = k_{id}\, t^{1/2} + I \tag{11}$$

where K_{id} is the intraparticle diffusion rate constant, Weber and Morris [64] have figured out the thickness of the

boundary layer from the values of *I*. Greater boundary layer effect was noticed with more significant intercept [65]. The plot of q_t vs. $t^{0.5}$ is presented in Fig. 15a. Usually, two separate linear portions represent each line observed. These two linear portions in the intraparticle model suggest that the removal process consists of both surface removal and intraparticle diffusion. While the first elongated part of the plot is the indicator of the existence of the boundary layer effect, the second linear portion is due to intraparticle diffusion [66]. In our case, only one linear part was obtained with outstanding R^2 value (0.9905), which indicates the exits of the boundary layer effect. The intraparticle diffusion rate (k_d), 0.7048 (mg/g min), calculated from the slope and the values of *C* (0.2975), the intercept, provides an idea about the thickness of the boundary layer. The larger the intercept, the higher is the boundary layer effect [65]. Accordingly, the boundary layer effect, in our case is minimal.

In case of involving the intraparticle diffusion in the sorption process, then a linear relationship would result from the plot of q_t vs. $t^{1/2}$, and the intraparticle diffusion would be the controlling step if this line passes through the origin [62]. Fig. 15a confirms that straight lines did not pass through the origin.

The diffusion rate equation inside particulate of Dunwald–Wagner can be expressed as [67] follows:

$$\log\left(1-F^2\right)=-\left(\frac{K}{2.303}\right)\times t \tag{12}$$

where *K* is the diffusion rate constant and the removal percentage, *F* is calculated by (q_t/q_e). The proper linear plot of log (1–F^2) vs. *t* (Fig. 15b) indicates the applicability of this kinetic model (R^2 0.9939). The value of the diffusion rate constant *K* for the Cr(VI) anions to the IONPs was found to be –0.418 min^{-1}. The linear line for the equation almost crosses the origin, indicating that the intraparticle diffusion is most probably the primary rate-controlling step [68]. This finding explains the slow rate of removal and the low removal percentage after 4 h of adsorption; 28%.

3.6. Adsorption thermodynamic studies

The effect of variation adsorption temperature was illustrated previously in Fig. 10. A positive impact of elevating the adsorption temperature of the Cr(VI) anions has been observed. Such finding is an indication of the endothermic nature of the Cr(VI) anions adsorption process on the IONPs adsorbent.

From engineering aspects, the values of thermodynamic parameters such as the enthalpy change ($\Delta H°$), the free energy change ($\Delta G°$) and the entropy change ($\Delta S°$) should be taken into consideration to conclude the spontaneity of the adsorption process. A spontaneous system will display a decrease in $\Delta G°$ and $\Delta H°$ values with increasing the temperature. All the thermodynamic parameters were calculated from the following equations [69,70]:

$$\ln K_0=\frac{\Delta S}{R}-\frac{\Delta H}{RT} \tag{13}$$

where:

$$K_0=\frac{q_e}{C_e} \tag{14}$$

$$\Delta G=-RT\ln K_0 \tag{15}$$

where *R* is the gas constant (8.314 J/mol K), and *T* is the temperature in K. Table 5 lists down the values for the thermodynamic parameters (Fig. 16). The positive value for the $\Delta H°$ (11.495 kJ/mol) indicates the endothermic nature of the process, which explains the increase of the Cr(VI) anions adsorption efficiency as the temperature increased. As informed by Alkan et al. [71], the enthalpy change values as a result of the chemisorption are between 40 and 120 kJ mol^{-1}, which are more significant than that caused by the physisorption. Consequently, the lower value of the heat of adsorption acquired in this study indicates that the adsorption of the Cr(VI) anions is probably attributable to the physisorption. Conversely, in the kinetics study, it was described that the adsorption is chemisorption. Thus, it is evident from the lower $\Delta H°$ value that the physisorption also takes part in the adsorption process in which the Cr(VI) anions adhere to the adsorbent surface only through weak intermolecular interactions. The positive value for the entropy change, $\Delta S°$ (21.875 J/mol K) illustrating the

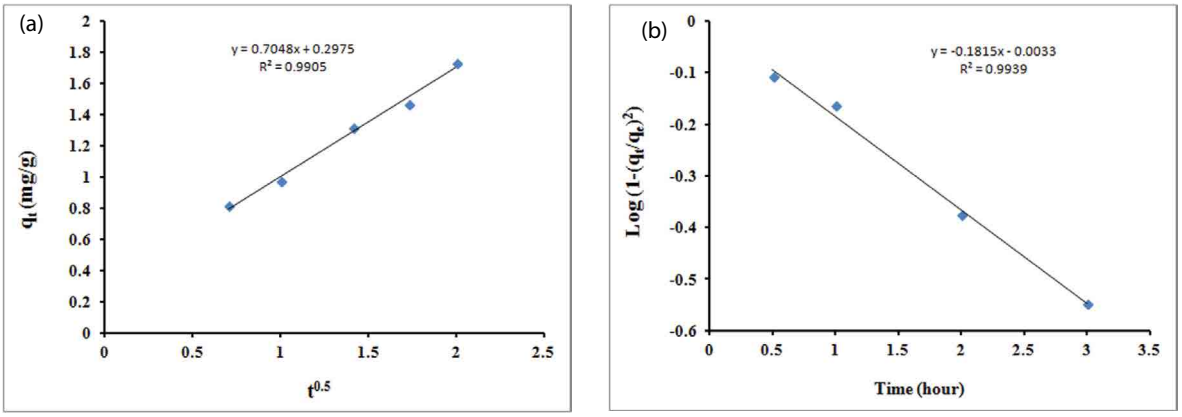

Fig. 15. Adsorption mechanism models: (a) intraparticle model and (b) Dunwald–Wagner model.

Table 5
Thermodynamic parameters of the Cr(VI) anions adsorption onto the IONPs under different temperatures

T	ΔG (kJ mol^{-1})	ΔH (kJ mol^{-1})	ΔS (J K^{-1} mol^{-1})
298	5.12	11.495	21.875
303	4.84		
308	4.64		
313	4.58		
318	4.495		

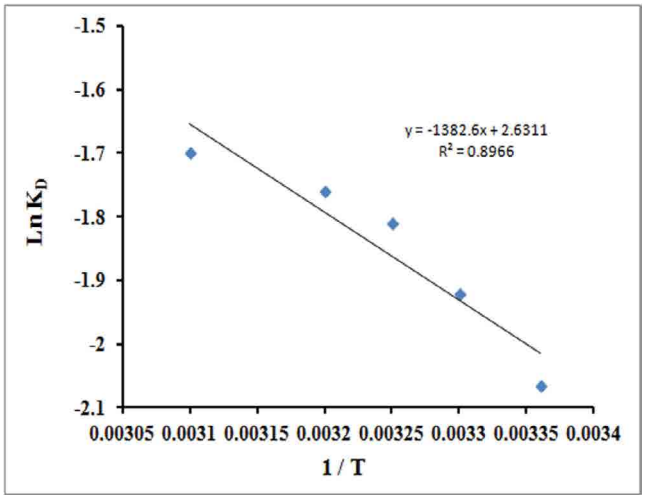

Fig. 16. Van't Hoff plot of the adsorption of the Cr(VI) ions on the IONPs.

disorderliness at the solid/liquid interface during the adsorption of the Cr(VI) anions onto the IONPs. The $\Delta G°$ values reflect the feasibility of the process.

3.7. Comparative study

The q_{max} values of Cr(VI) by different adsorbents from the literature reports compared with IONPs (this study) shown in Table 6. The IONP adsorbent showed a higher q_{max} value of Cr(VI) than some adsorbents reported earlier, such as various AC adsorbents [72–74], and even more top than iron oxide and maghemite nanoparticles [38,41]. However, it was lower than some other adsorbents [75,76]. The discrepancy of q_{max} values for Cr(VI) among adsorbents could be attributed to the different solutions chemistry and affinities of the adsorbent for Cr(VI). Overall, the q_{max} of IONP adsorbent for Cr(VI) was in a moderate range compared with the other adsorbents. The IONPs adsorbent can rapidly be separated from the water by installing a magnetic separator in the adsorption process and then collected from the treatment system. The adsorption capacity of contaminants such as dyes by IONPs improved by the development of a novel adsorbent, Fe–Mn–Zr metal oxide nanocomposite [77] where enhanced adsorption capacities of 196.07 and 175.43 mg/g observed for MO and EY dye, respectively, due to synergistic effects of physicochemical properties of tri-metal oxides.

Table 6
Comparative study of the Cr(VI) ions adsorption capacity by conventional adsorbents

Adsorbent	q_{max} (mg/g)	Reference
Sawdust	1.90	[72]
Granular activated carbon	0.99	[73]
Activated carbon	0.571	[74]
Hexadecyltrimethylammonium bromide-modified activated carbon	1.82	[74]
Cetylpyridinium chloride-modified activated carbon	1.66	[74]
Iron oxide nanoparticles	2.39	[38]
Maghemite nanoparticles	2.36	[41]
Magnetite nanoparticles	20.20	[75]
Fe-modified AC from *Trapa natans* husk	11.83	[76]
Iron oxide nanoparticles	2.75	This study

A novel magnetic mesoporous adsorbent with a mixed phase of Fe_2O_3/Mn_3O_4 nanocomposite was developed and used as an adsorbent for toxic methyl orange (MO) dye removal. The maximum adsorption capacity of this nanocomposite was found to be 322.58 mg/g from the Langmuir isotherm model [78].

A mixed-phase of $CaFe_2O_4$ and ZrO_2 magnetic nanocomposite (CaF-ZO-MNC) was developed and explored for reduction of methyl orange (MO) dye from an aqua matrix. Enhanced adsorption capacity towards MO dye was found to be 370.37 mg/g from the Langmuir model, which is higher than standalone nanoscale Fe, Ca and Zr metal oxide nanoparticles [79].

Nanoparticles of α-Fe_2O_3 were synthesized by simple chemical precipitation method and investigated for adsorptive removal of methyl orange (MO) dye from aqueous solution. A maximum adsorption capacity as much as 28.90 mg/g is reported [80].

Mixed phase crystalline hausmannite and manganese ferrite nanoparticles with magnetic properties were developed and used as an adsorbent for removal of toxic dye reactive orange (RO) from water, and its easy magnetic separation process was explored and a maximum adsorption capacity as much as 200 mg/g was reported [81].

4. Conclusion

In this study, IONPs were developed by alginate hydrogel template for chromium (VI) ions separation. The separation efficiency of the IONPs for Cr(VI) ions from aqueous solution was investigated under different operational conditions. It was found that increase in the initial Cr(VI) ions concentration positively affected the adsorption capacity up to 40 mg/L where the saturation of the IONPs was noticed. In the contrary, the increase of the solution's pH negatively affected the adsorption capacity. The adsorbent dosage influenced the adsorption capacity in a slightly appositive manner with increasing the dose up to 0.1 g where the maximum adsorption capacity was recognized; 2.32 mg/g.

A fast decline has been observed with the further increase of the adsorbent dose. A linear relation has been seen with increasing the contact time up to 4 h. The same behaviour was observed with an elevation of the adsorption's temperature up to 35°C then the slower rate has been obtained with a further elevation of the temperature. Different particles size has been received by altering the calcination temperature. An inversely proportional relation between the IONPs and the adsorption capacity has been established. Furthermore, the adsorption process data were best fitted using pseudo-first-order, pseudo-second-order and Elovich kinetic models. The isotherm nature of the adsorption process was found to follow the classical monolayer Langmuir isotherm model. The maximum monolayer adsorption capacity was found to be 2.75 mg/g. The boundary layer effect was found slightly controlling step of the adsorption process according to the inter-particles diffusion model while the intraparticle diffusion is most probably the primary rate-controlling step according to the D-W diffusion model. This finding explains the slow rate of removal and the low removal percentage after 4 h of adsorption; 28%. The thermodynamic parameters of the adsorption process indicated an endothermic nature. Finally, the IONPs were characterized using FT-IR, TGA, SEM, TEM, XRD and magnetic properties analysis.

References

[1] Y. Yu, K. Hubacek, K. Feng, D. Guan, Assessing regional and global water footprints for the UK, Ecol. Econ., 69 (2010) 1140–1147.

[2] N.R. Mizyed, Challenges to treated wastewater reuse in arid and semi-arid areas, Environ. Sci. Policy, 25 (2013) 186–195.

[3] R. Khlifi, H. Chaffai, Head and neck cancer due to heavy metal exposure via tobacco smoking and professional exposure: a review, Toxicol. Appl. Pharmacol., 248 (2010) 71–88.

[4] S. Babel, T.A. Kurniawan, Low-cost adsorbents for heavy metals uptake from contaminated water: a review, J. Hazard. Mater., 97 (2003) 219–243.

[5] G. Khitrov, R. Jaeger, Chromium Toxicity, The Ronald O. Perlman Department of Dermatology, Department of Toxicology NYU Grad School of Arts and Science. Available: http://www.nyu.edu/classes/jaeger/chromium_toxicity.htm. (Accessed 20 November 2013).

[6] M. Bhaumik, A. Maity, V.V. Srinivasu, M.S. Onyango, Enhanced removal of Cr(VI) from aqueous solution using polypyrrole/Fe_3O_4 magnetic nanocomposite, J. Hazard. Mater., 190 (2011) 381–390.

[7] W.S. Wan Ngah, H. Makm, Removal of heavy metal ions from wastewater by chemically modified plant wastes as adsorbents: a review, Bioresour. Technol., 99 (2008) 3935–3948.

[8] M. Barakat, New trends in removing heavy metals from industrial wastewater, Arab. J. Chem., 4 (2011) 361–377.

[9] W. Büchner, R. Schliébs, G. Winter, K.H. Bucjel, Primary Inorganic Materials, In D.H. Dyllick-Brenzinger, Industrial Inorganic Chemistry, 1989, pp. 8–12, Verlagsgesellschaft, New York.

[10] M. Mahmoudi, S. Sant, B. Wang, S. Laurent, T. Sen, Superparamagnetic iron oxide nanoparticles (SPIONs): development, surface modification and applications in chemotherapy, Adv. Drug Delivery Rev., 63 (2011) 24–46.

[11] S.A. Al-Saydeh, M.H. El-Naas, S.J. Zaidi, Copper removal from industrial wastewater: a comprehensive review, J. Ind. Eng. Chem., 56 (2017) 35–44.

[12] P. Khanna, C. Ong, B. Bay, G. Baeg, Nanotoxicity: an interplay of oxidative stress, inflammation and cell death, Nanomaterials, 5 (2015) 1163–1180.

[13] A.S. Teja, P.Y. Koh, Synthesis, properties, and applications of magnetic iron oxide nanoparticles, Prog. Cryst. Growth Charact. Mater., 55 (2009) 22–45.

[14] A.M. Seid-Mohammadi, Gh. Asgari, M.T. Sammadi, M. Ahmadian, A. Poormohammadi, Removal of humic acid from synthetic water using chitosan as coagulant aid in electrocoagulation process for Al and Fe electrodes, Res. J. Chem. Environ., 18 (2014) 19–25.

[15] M.M. Sagrario, L.A. Gracia-Cerda, T.J.R. Lubian, Preparation and characterization of cobalt ferrite by the polymerized complex method, Mater. Lett., 59 (2005) 1056–1060.

[16] B.R. Galindo, A.O. Valenzuela, L.A. Gracia-Cerda, R.O. Fernandez, M.J. Aquino, G. Ramos, Y.H. Madeira, Synthesis and magneto-structural study of $Co_xFe_{3-x}O_4$ nanoparticles, J. Magn. Mag. Mater., 294 (2005) e33–e36.

[17] Z.L. Liu, X. Wang, K.L. Yao, G.H. Du, Q.H. Lu, Z.H. Ding, J. Tao, Q. Ning, X.P. Luo, D.Y. Tian, D. Xi, Synthesis of magnetite nanoparticles in W/O microemulsion, J. Mater. Sci., 39 (2004) 2633–2636.

[18] P.A. Dresco, V.S. Zaitsev, R.J. Gambino, B. Chu, Preparation and properties of magnetite and polymer magnetite nanoparticles, Langmuir, 15 (1999) 1945–1951.

[19] K. Sunderland, P. Brunetti, L. Spinu, J. Fang, Z. Wang, W. Lu, Synthesis of γ-Fe_2O_3/polypyrrole nanocomposite materials, Mater. Lett., 58 (2004) 3136–3140.

[20] L.A. Gracia-Cerda, R. Chapa-Rodriguez, J. Bonilla-Rios, *In situ* synthesis of iron oxide nanoparticles in a styrene-divinylbenzene copolymer, Polym. Bull., 58 (2007) 989–994.

[21] H. Lin, Y. Watanabe, M. Kumura, K. Hanabusa, H. Shirai, Preparation of magnetic poly(vinyl alcohol) (PVA) materials by in situ synthesis of magnetite in a PVA matrix, J. Appl. Polym. Sci., 87 (2003) 1239–1247.

[22] P.S. Chowdhury, P.R. Arya, K. Raha, Green synthesis of nanoscopic iron oxide particles: a potential oxidizer in nanoenergetics, Synth. React. Inorg. Met., 37 (2007) 447–451.

[23] D.M. Kim, M. Mikhaylova, F.H. Wang, J. Kehr, B. Bjelke, Y. Zhang, T. Tsakalakos, M. Muhammed, Starch-coated superparamagnetic nanoparticles as MR contrast agents, Chem. Mater., 15 (2003) 4343–4351.

[24] Y.-Y. Liang, L.-M. Zhang, W. Li, Polysaccharide-modified iron oxide nanoparticles as an effective magnetic affinity adsorbent for bovine serum albumin, Colloid Polym. Sci., 285 (2007) 1193–1199.

[25] O. Carp, D. Visinescu, G. Patrinoiu, A. Tirsoaga, Green synthetic strategies of oxide materials: polysaccharides-assisted synthesis. Part IV. Alginate-assisted synthesis of nanosized metal oxides, Rev. Roum. Chim., 56 (2011) 901–906.

[26] S. Plumejeau, J.G. Alauzun, B. Boury, Hybrid metal oxide@ biopolymer materials precursors of metal oxides and metal oxide-carbon composites, Ceram. Soc. Jpn., 123 (2015) 695–708.

[27] A. Ali, H. Zafar, M. Zia, I. ul Haq, A.-R. Phull, J.S. Ali, A. Hussain, Synthesis, characterization, applications, and challenges of iron oxide nanoparticles, Nanotechnol. Sci. Appl., 9 (2016) 49–67.

[28] M. Nidhin, R. Indumathy, K.J. Sreeram, B. Unninair, Synthesis of iron oxide nanoparticles of narrow size distribution on polysaccharide templates, Bull. Mater. Sci., 31 (2008) 93–96.

[29] S.K. Janardhanan, I. Ramasamy, B. Unni Nair, Synthesis of iron oxide nanoparticles using chitosan and starch templates, Trans. Met. Chem., 33 (2008) 127–131.

[30] S. Chen, J. Feng, X. Guo, J. Hong, W. Ding, One-Step Wet Chemistry for Preparation of Magnetite Nano-rods, Mater. Lett., 59 (2005) 985–988.

[31] S. Basavaraja, D.S. Balaji, M.D. Bedre, Solvothermal synthesis and characterization of acicularα-Fe_2O_3 nanoparticles, Bull. Mater. Sci., 34 (2011) 1313–1317.

[32] J.A. Gadsden, Infrared Spectra of Minerals and Related Inorganic Compounds, Butterworths Publ., England, 1975.

[33] J. Coates, Interpretation of Infrared Spectra, A Practical Approach, Encyclopedia of Analytical Chemistry, A. Meyers, Ed., John Wiley & Sons Ltd., Chichester, 2000, p. 10815.

[34] V.C. Farmer, The Infrared Spectra of Minerals, Mineralogical Society, London, 1974, p. 539.

[35] M.M. Rahman, S.B. Khan, A. Jamal, Iron Oxide Nanoparticles, Intech Open access publisher, 2011, p. 43.
[36] T.M. Tamer, W.M. Abou-Taleb, G.D. Roston, M.S. Mohyeldin, A.M. Omer, E.F. Shehata, Characterization and evaluation of iron oxide nanoparticles prepared using hydrogel template based on phosphonate alginate, Nanosci. Nanotechnol.-Asia, 7 (2017) 220–232.
[37] M. Hua, Heavy metal removal from water/wastewater by nanosized metal oxides: a review, J. Hazard. Mater., 211–212 (2012) 317–331.
[38] D. Kitkaew, A. Phetrak, S. Ampawong, R. Mingkhwan, D. Phihusut, K. Okanurak, C. Polprasert, Fast and efficient removal of hexavalent chromium from water by iron oxide particles, Environ. Nat. Resour. J., 16 (2018) 91–100.
[39] D.S. Shirsath, B.N. Patil, V.S. Shrivastava, Development of new technology for the removal of Cr^{6+} by magnetic nanoadsorbents from the industrial or sewage wastewater, J. Mater. Environ. Sci., 9 (2018) 1969–1978.
[40] K.A. Al-Saad, M.A. Amr, D.T. Hadi, R.S. Arar, M.M. AL-Sulaiti, T.A. Abdulmalik, N.M. Alsahamary, J.C. Kwak, Iron oxide nanoparticles: applicability for heavy metal removal from contaminated water, Arab. J. Nucl. Sci. Appl., 45 (2012) 335–346.
[41] B. Lkhagvadulam, B. Tsagaantsetseg, D. Tergel, S. Chuluunkhuyag, Removal of chromium from a tannery wastewater by using a maghemite nanoparticles, Int. J. Environ. Sci. Dev., 8 (2017) 696–702.
[42] R. Ansari, Application of polyaniline and its composites for adsorption/recovery of chromium (VI) from aqueous solutions, Acta Chim. Slov., 53 (2006) 88–94.
[43] P. Yuan, Removal of hexavalent chromium [Cr(VI)] from aqueous solutions by the diatomite-supported/unsupported magnetite nanoparticles, J. Hazard. Mater., 173 (2010) 614–621.
[44] R. Chen, L. Chai, Q. Li, Y. Shi, Y. Wang, A. Mohammad, Preparation and characterization of magnetic Fe_3O_4/CNT nanoparticles by RPO method to enhance the efficient removal of Cr(VI), Environ. Sci. Pollut. Res. Int., 20 (2013) 7175–7185.
[45] H.I. Adegoke, F.A. Adekola, O.S. Fatoki, B.J. Ximba, Adsorption of Cr (VI) on synthetic hematite (α-Fe_2O_3) nanoparticles of different morphologies, Korean J. Chem. Eng., 31 (2013) 142–154.
[46] S. Ramasubramaniam, C. Govindarajan, T. Gomathi, P.N. Sudha, Removal of Chromium (VI) from aqueous solution using chitosan -Starch blend, Der Pharm. Lett., 4 (2012) 240–248.
[47] Y.F. Shen, J. Tang, Z.H. Nie, Y.D. Wang, Y. Ren, L. Zuo, Preparation and application of magnetic Fe_3O_4 nanoparticles for wastewater purification, Sep. Purif. Technol., 68 (2009) 312–319.
[48] F. Rozada, L.F. Calvo, A.I. Garcia, J. Martin-Villacorta, M. Otero, Dye adsorption by sewage sludge-based activated carbons in batch and fixed-bed systems, Bioresour. Technol., 87 (2003) 221–230.
[49] G. Gode, E. Pehlivan, Adsorption of Cr(III) ions by Turkish brown coals, Fuel Process. Technol., 86 (2005) 875–884.
[50] Y.S. Ho, Effect of pH on lead removal from water using tree fern as the sorbent. Bioresour. Technol., 96 (2005) 1292–1296.
[51] M.M. Dubinin, E.D. Zaverina, L.V. Radushkevich, Sorption and structure of active carbons I. adsorption of organic vapors, Zhurnal Fizicheskoi Khimii, 21 (1947) 1351–1362.
[52] N. Unlü, M. Ersoz, Adsorption characteristics of heavy metal ions onto a low cost biopolymeric sorbent from aqueous solutions, J. Hazard. Mater., 136 (2006) 272–280.
[53] A. Mohammad, A.K.R. Rifaqat, A. Rais, A. Jameel, adsorption studies on citus reticulate (fruit peel of orange): removal and recovery of Ni (II) from electroplating wastewater, J. Hazard. Mater., 79 (2000) 117–131.
[54] A. Stolz, Basic and applied aspects in the microbial degradation of azo dyes, Appl. Microbiol. Biotechnol., 56 (2001) 69–80.
[55] B.H. Hameeda, L.H. China, S. Rengarajb, Adsorption of 4-chlorophenol onto activated carbon prepared from rattan sawdust, Desalination, 225 (2008) 185–198.
[56] M.I. Temkin, V. Pyzhev, Kinetics of ammonia synthesis on promoted iron catalyst, Acta Physiochim. URSS, 12 (1940) 327–356.
[57] I.A.W. Tan, A.L. Ahmad, B.H. Hameed, Adsorption isotherms, kinetics, thermodynamics and desorption studies of 2,4,6-trichlorophenol on oil palm empty fruit bunch-based activated carbon, J. Hazard. Mater., 164 (2009) 473–482.
[58] M. Ozacar, I.A. Sengil, A kinetic study of metal complex dye sorption onto pinedust, Process Biochem., 40 (2005) 565–572.
[59] P.K. Pandey; S.K. Sharma; S.S. Sambi, Kinetics and equilibrium study of chromium adsorption on zeoliteNaX, Int. J. Environ. Sci. Technol., 7 (2010) 395–404.
[60] M. Barkat, D. Nibou, S. Chegrouche, A. Mellah, Kinetics and thermodynamics studies of chromium(VI) ions adsorption onto activated carbon from aqueous solutions, Chem. Eng. Process. Process Intensif., 48 (2009) 38–47.
[61] R.L. Tseng, Mesopore control of high surface area NaOH-activated carbon, J. Colloid Interface Sci., 303 (2006) 494–502.
[62] G. Crini, H.N. Peindy, F. Gimbert, C. Robert, Removal of C. I. Basic Green 4 (malachite green) from aqueous solutions by adsorption using cyclodextrin-based adsorbent: kinetic and equilibrium studies, Sep. Purif. Technol., 53 (2007) 97–110.
[63] G. McKay, The adsorption of dyestuffs from aqueous solution using activated carbon: analytical solution for batch adsorption based on external mass transfer and pore diffusion, Chem. Eng. J., 27 (1983) 187–195.
[64] W.J. Weber, J.C. Morris, Kinetics of adsorption on carbon from solution, J. Sanity, Eng. Div. Am. Soc. Civil. Eng., 89 (1963) 31–59.
[65] K. Kannan, M.M. Sundaram, Kinetics and mechanism of removal of methylene blue by adsorption on various carbons—a comparative study, Dyes Pigm., 51 (2001) 25–40.
[66] M. Sarkar, P.K. Acharya, B. Bhaskar, Modeling the removal kinetics of some priority organic pollutants in water from diffusion and activation energy parameters, J. Colloid Interface Sci., 266 (2003) 28–32.
[67] G. McKay, M.S. Otterburn, J.A. Aja, Fuller's earth and fired clay as adsorbents for dye stuffs, Water Air Soil Pollut., 24 (1985) 307–322.
[68] S.K. Abdul Karim, S.F. Lim, S.N. David Chua, S.F. Salleh, P.L. Law, Banana fibers as sorbent for removal of acid green dye from water, J. Chem., 2016 (2016) 1–11.
[69] T.A. Khan, S. Dahiya, I. Ali, Use of kaolinite as adsorbent: equilibrium, dynamics and thermodynamic studies on the adsorption of Rhodamine B from aqueous solution, Appl. Clay Sci., 69 (2012) 58–66.
[70] G. Zhao, J. Li, X. Wang, Kinetic and thermodynamic study of 1-naphthol adsorption from aqueous solution to sulfonated graphene nanosheets, Chem. Eng. J., 173 (2011) 185–190.
[71] M. Alkan, O. Demirbas, S.Ç.M. Dogan, Sorption of acid red 57 from aqueous solution onto sepiolite, J. Hazard. Mater., B116 (2004) 135–145.
[72] N.K. Hamadi, X.D. Chen, M.M. Farid, M.G.Q. Lu, Adsorption kinetics for the removal of chromium(VI) from aqueous solution by adsorbents derived from used tyres and sawdust, Chem. Eng. J., 84 (2001) 95–105.
[73] H.-D. Choi, J.-M. Cho, K. Baek, J.-S. Yang, J.-Y. Lee, Influence of cationic surfactant on adsorption of Cr(VI) onto activated carbon, J. Hazard. Mater., 161 (2009) 1565–1568.
[74] H.-D. Choi, W.-S. Jung, J.-M. Cho, B.-G. Ryun, J.-S. Yang, K. Baek, Adsorption of Cr(VI) onto cationic surfactant-modified activated carbon, J. Hazard. Mater., 166 (2009) 642–646.
[75] S. Rajput, C.U. Pittman, D. Mohan, Magnetic magnetite (Fe_3O_4) nanoparticle synthesis and applications for lead (Pb^{2+}) and chromium (Cr^{6+}) removal from water, J. Colloid Interface Sci., 468 (2016) 334–346.
[76] W. Liu, J. Zhang, C. Zhang, Y. Wang, Y. Li, Adsorptive removal of Cr (VI) by Fe-modified activated carbon prepared from *Trapa natans* husk, Chem. Eng. J., 162 (2010) 677–684.
[77] N.H. Singh, K. Kezo, A. Debnath, B. Saha, Enhanced adsorption performance of a novel Fe-Mn-Zr metal oxide nanocomposite adsorbent for anionic dyes from binary dye mix: response surface optimization and neural network modeling, Appl. Organometal Chem., 32 (2018) e4165.
[78] M. Bhowmik, K. Deb, A. Debnath, B. Saha, Mixed phase Fe_2O_3/Mn_3O_4 magnetic nanocomposite for enhanced adsorption of

methyl orange dye: neural network modeling and response surface methodology optimization, Appl. Organometal Chem., 32 (2018) e4186.
[79] M. Bhowmik, A. Debnath, B. Saha, Fabrication of mixed phase calcium ferrite and zirconia nanocomposite for abatement of methyl orange dye from aqua matrix: optimization of process parameters, Appl. Organometal Chem., 32 (2018) e4607.
[80] A. Debnatha, K. Deb, K.K. Chattopadhyay, Biswajit Saha, Methyl orange adsorption onto simple chemical route synthesized crystalline α-Fe_2O_3 nanoparticles: kinetic, equilibrium isotherm, and neural network modeling, Desal. Wat. Treat., 57 13549–13560.
[81] N.H. Singh, A. Bera, A. Debnath, B. Saha, Mixed phase crystalline hausmannite and manganese ferrite nanoparticles with magnetic properties for environmental application, Mater. Today Proc., 5 (2018) 2300–2305.